Spacecraft Line-of-sight Stabilization using LWIR Earth Signature

Marco B.Quadrelli[1] and Sabino Piazzolla.[2]
Jet Propulsion Laboratory, California Institute of Technology, 4800 Oak Grove Drive, Pasadena, CA 91109

The objective of this study is to investigate the potential of using the bright and near-uniform Earth thermal infrared (or long wavelength infrared, LWIR) signature as a stable reference for accurate (micro-rad or less) inertial pointing and tracking on-board an space vehicle, including the determination of the fundamental limits of applicability of the proposed method for space missions. We demonstrate sub-micro radian level pointing accuracy under a representative set of disturbances experienced by the spacecraft in orbit.

I. Introduction

In this paper we investigate the potential of using the bright and near-uniform Earth thermal infrared (or long wavelength infrared, LWIR) signature as a stable reference for accurate (micro-rad or less) inertial pointing and tracking of an optical communication beacon on-board an space vehicle, including the determination of the fundamental limits of applicability of the proposed method for space missions in LEO and deep space. In the thermal Infrared Earth's emission appears relatively uniform and it is independent of the Sun Illumination. Therefore it can be used as a stable pointing reference.

Up to the present time, when a space vehicle requires a reference signal for inertial pointing the choices are: a signal beacon from an Earth location, the Earth radiance in the visible, or a star tracker. However, limitations can arise from using the above techniques. For example, the signal beacon suffers from limited signal power (either in RF or optical) and will constrain the application to limited ranges, errors due to stray-light and centroiding limit the accuracy of a star tracker, and the spatial/temporal variability of the Earth's albedo and its illumination by the Sun introduces limitations when used in the visible or near infrared. To by-pass these limitations, we consider to use the bright and near-uniform image of the Earth in the LWIR (8-13 μm), Fig. 1, to obtain a reference signal for inertial stabilization and pointing of a spacecraft platform. Advantages in using this approach are twofold: the radiance of Earth in the LWIR is not only much more uniform and with less variability compared to the one in the visible, as shown in Figure 1, but its radiance is near independent of the Sun illumination phase [1], with the consequence that the emission of the Earth in the thermal infrared is roughly

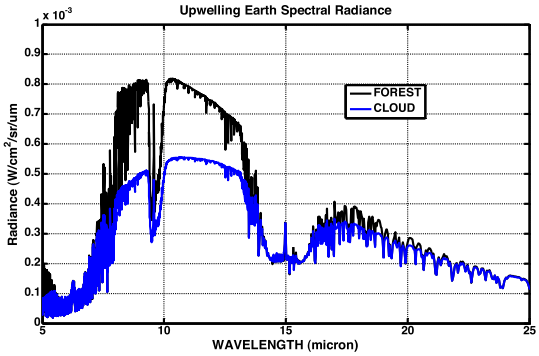

Figure 1. (Top) Image of the Earth in the visible and thermal infrared. (Bottom) Earth radiance in the thermal infrared: the radiance upwelling radiance corresponding to a forest and cloud coverage. Data obtained after MODTRAN simulation.

[1] corresponding author, Senior Engineer, Robotic Modeling, Simulation, and Visualization Group, Autonomous Systems Division, Mail Stop 198-219, marco.b.quadrelli@jpl.nasa.gov, senior AIAA Member.
[2] Optical Communications Group, Mail Stop 161-135.

constant in all directions, making it an excellent candidate for inertial referencing, as depicted in Fig. 1.

In this study we begin the development of pointing and tracking algorithms that make use of the Earth signal in the LWIR spectrum as a reference as shown in Figure 2. This development is relatively new and represents a concept that has not yet been explored in sufficient detail. The proposed approach takes into consideration the LWIR signal from Earth, and develops centroiding algorithms of the Earth image in LWIR. Because of the Earth radiance data, as shown in Figure 2, Earth images will be reconstructed using the simulated performance of different array detectors and their noise models [2].

This study is not tied to any particular project, rather is an analytical assessment of feasibility. Hence, the data is purely representative of plausible behavior. For instance, we use Mars Reconnaissance Orbiter (MRO) telemetry data to synthesize a disturbance profile that has to be filtered out to achieve the intended sub-microradian pointing accuracy. Also, MRO structural modal data was not available, hence a representative modal spectrum and structural damping levels were derived to represent the platform structural response.

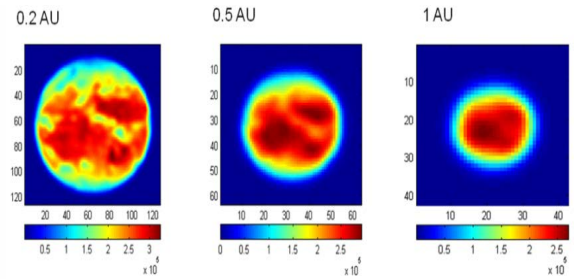

Figure 2. The brightness and near-uniformity of the Earth LWIR signature as a function of range indicates its great potential as a stable reference for inertial pointing of planetary spacecraft, also when the Earth is not fully illuminated by the Sun. Earth image reconstructed by AIRS satellite measurement data.

A sensitivity analysis on the imaging sensor will illustrate limitations and recommendations on allowable Earth reference signal (e.g. aperture of the optics collecting area) at various ranges (see Fig. 2) and thermal infrared sensor noise and pixellation level required for effective signal tracking as a function of orbital distance.

The outline of the remainder of this article is as follows. Section II describes the assumptions of the model used in the simulation. Section III describes the process of detection of the Earth's image, and the centroiding technique. Section IV summarizes the development of the dynamic model, base body control, and LOS control. Section V discusses the external disturbances. Section VI summarizes the properties of the dynamic isolation filter. Section VII discusses the simulation results, and Section IX concludes the paper.

II. Assumptions of model used for Line-of-Sight Stabilization

Objective of the stabilization is to align the Earth's image along the desired LOS in the face of existing system disturbances.

Because of the submicro-radian precision levels required by high precision pointing, a large dynamic range is involved in the dynamic response of the pointing system.

Hence, the pointing and tracking algorithms are based on a multistage approach, which includes:

- a coarse stage (outer loop) based on sequential loop closure of a vehicle attitude stabilization feedback control loop at a low control bandwidth (1e-3 to 1e-1 Hz) to compensate for typical attitude control disturbances, followed by
- a fine stage (inner loop) based on an image bore-sight stabilization feedback loop at higher frequencies which makes use of an articulated (tip/tilt) fast steering mirror to track the Earth's LWIR reference signal in the image plane.

Figure 3 describes the problem under consideration. The spacecraft follows an orbital path (could be around any planet) and points a gimbaled payload to a spot on the Earth. The

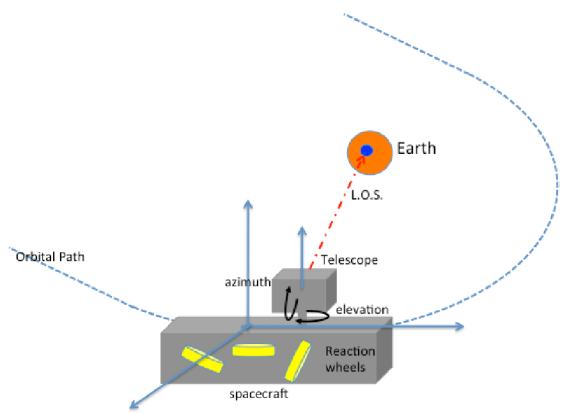

Figure 3. Depiction of problem under consideration. The spacecraft follows an orbital path (could be around any planet) and points a gimbaled payload to a spot on the Earth. The azimuth and elevation angles are the states of the gimbaled payload and are the states to be tracked and stabilized upon in the model used in this study.

azimuth and elevation angles are the states of the gimbaled payload and are the states to be tracked and stabilized upon in the model used in this study. They define the line-of-sight (LOS). The spacecraft is acted upon by a set of disturbances, and the representative disturbances used in this study are due to a set of three reaction wheel actuators. These actuators stabilize the spacecraft with respect to inertial space. The gimbal moves the telescope (payload) with respect to the spacecraft (base body) so as to track the LOS. In reality, there is an optical bench with components such as fine steering and scanning mirrors which track and stabilize the LOS at high bandwidths, but in this study we ignore this level of detail and assume that what is being pointed is a two-state system (in azimuth and elevation) being pointed with respect to a reference direction (LOS), assumed to be the origin of the image plane (zero-reference).

Regarding the degree of accuracy required by the pointing system, we can make the following considerations. Assuming for example the case of a hypothetical mission carrying an optical communication payload with an aperture a 20cm, if the downlink wavelength is 1550 nm, the related diffraction limited beam width (according to the approximation λ/D, is of the order of 7.5 micro-rad. The resulting pointing error of the downlink beam must be a fraction of the beam width, which is of the order of submicro-radian.

The approach under investigation includes the preliminary modeling of the disturbances caused by orbital dynamics and sensor (star tracker noise, gyro drift and random walk) and actuator (reaction wheel noise, thruster noise and quantization) noise. Solutions will be proposed for disturbance rejection of these noise sources to achieve a desired centroiding accuracy/stability compatible with deep space missions including optical communication scenarios with pointing accuracies in the micro-radian level or less.

Summarizing, the assumptions of the simulation model used in this study are the following:

- Small spacecraft angles considered (no platform translation dynamics for now)
- Disturbances modeled: base body noise, reaction wheels, gyro noise, no thruster firings
- Representative LOS control: 100 Hz BW, 1000 Hz sampling rate
- Errors due to thermal, orbital ephemeris, and GPS are zero for now
- Target in simulation is assumed to be inertially-fixed
- Gimbaled payload is represented by an equivalent rigid body moving in azimuth and elevation (tip/tilt) to track the centroid of the Earth's image
- Spectral separation invoked between inner loop and outer loop, which assumes that an ideal dynamic isolation stage has achieved this decoupling.
- No consideration of point-ahead angle, or payload steering.
- No consideration of thermal management issues for the detector.
- Earth's emission in the LWIR range and telescope aperture 20 cm.

III. Detection of Earth Image and Centroiding Algorithm

In the proposed simulation and in real applications as well, the tasks to perform are the following ones:

1) The image of the Earth is acquired by the detector array on the focal plane.

2) An algorithm derives the centroiding of position of the Earth in the focal plane.

3) The Earth's centroiding at the focal plane are transformed in angular position of the Earth respect to the axis of the telescope (azimuth and elevation angle) and sent to the spacecraft control system

4) The control system of the spacecraft once acquired the information of the position of the Earth moves gradually the telescope axis to align it with Earth (e.g. the Earth must be at the center of the focal plane of the telescope).

5) The control system of the spacecraft stabilize the Earth position and filter out mechanical noise and sensor noise (Line of Sight Stabilization).

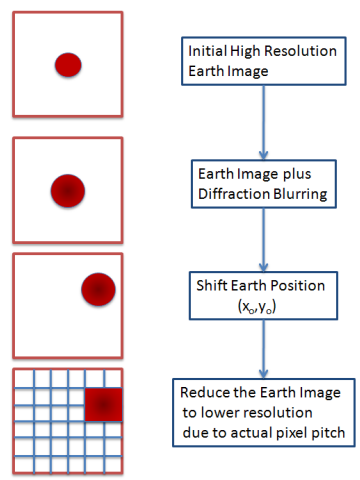

Figure 4. Initial algorithm to capture the image of Earth in a low resolution pixel array.

The first task to accomplish is the detection of the Earth's image by the detector array (sensitive in the LWIR range) located at the focal plane of the optical system and then the application of an algorithm able locate the position of the Earth center in the focal plane array. To do so, in this work, it was considered to implement a flexible software program able to ingest input values in such a way that can be easily varied when a parametric simulation is required. The simulation described here can be divided in two steps, first image detection and acquisition on the pixel array of the Earth image and then Earth centroiding. All the algorithms for the simulation proposed are implemented using MATLAB programming language [3].

A. Simulation of Earth Detection and Acquisition

The purpose of the detection and centroiding algorithm is to 1) detect the image of the Earth images in the focal plane, 2) transmit the position of the detected Earth in the focal plane, or the centroiding $\{x_o, y_o\}$ describing the position of the center of Earth, to the LOS system. To do so, the simulation first creates an images at the pixellated focal plane of the system, then counts the distribution of the photoelectrons in the image plane, finally applies a centroiding algorithm to derive the Earth position $\{x_o, y_o\}$ in the focal plane. It must be taken into account that a number of disturbances affects the accuracy of the centroiding calculation, including the sensor noise, the pixellation of the image, background and stray light radiation etc. A centroiding algorithm must be able to mitigate the effects of the noise and therefore to reduce the centroiding errors associated to the calculation.

As discussed in the Introduction, the Earth image in the LWIR spectrum appears generally uniform, therefore it was considered, as a first approach, to simulate the Earth as a uniform disc that is radiating at given spectral radiance (dimensionally, in $W/cm^2/sr/\mu m$).

The aperture of the optical system determines, along with the system field of view and the system spectral bandwidth, the Earth signal (photon flux) captured. In our case, to keep the system aperture comparable in size to other systems that have been considered for other deep space missions, an initial assessment of an optical system with aperture of 20 cm of diameter with focal length of 300 cm. Once the system aperture and f-number is selected, it is relatively simple to calculate the size of the Earth disc at the focal plane. Diffraction effects are also included to properly render the Earth image on the focal plane.

Great care must be taken when imaging the Earth disc on a detector array. Usually, a detector array can have pixel pitch that varies form few to tens of microns. It will be erroneous, therefore, in a simulation to try to 'directly' capture the image of Earth at this resolution. In fact, if one wants to resolve via software the signal from Earth using such pixel pitch, a large round-off error can be created that in first instance affects the centroiding calculation. To capture correctly the Earth image by a 'coarse' detector array, a different simulation approach was used, as described in Fig. 4. In our simulation approach, first the image of Earth is created at the center of an hypothetical focal plane using a pixel array having (high) resolution much larger than the actual array used in the focal plane (e.g. 100 times), having the all other conditions of the optical system left the same. The initial Earth image is positioned at the center. Each pixel of this high-resolution array has same quantum efficiency of the actual low resolution array and the exposure time of the image is the same of that one required by the system. During the given exposure time, each pixel of the high definition image captures a number of photoelectrons. The total number of photoelectrons is the strength of the Earth signal. After this stage to complete the physical rendering of the image, the Earth image experiences the blurring effect due to diffraction and the image will be increased in size (with the same total photoelectron count), as shown in Figure 4. Then the image is shifted in the focal plane, with centroiding $\{x_o, y_o\}$. In this way we obtain the image of the Earth at higher resolution located in the actual position in the detector array. After this phase, the content of the high-resolution pixel array can be transformed via software in an image (at lower resolution) corresponding the actual detector array. Again the total photoelectron count of the Earth in this image of low resolution (higher pixel pitch) is the same of the initial high-resolution image.

B. Earth Centroiding Algorithm

Once the Earth's image is defined on the actual pixel array, the determination of centroids of the Earth's image can start as illustrated Fig. 5. However, before to proceed with the actual centroiding algorithm, sensor noise must be added as a possible photoelectron background count to each pixel. The origin of this added noise can be twofold. First, stray-light due to the proximity of the telescope to the Sun can generate, because of contamination scattering and mirror roughness, an additional background radiation at the focal plane. Next, the thermal infrared emission of the optical elements (at temperature different from zero Kelvin) in the optical path may add up in the focal plane [2]. At the moment we have not considered a detailed analysis of the background behavior. Instead we

prefer to add the background count directly in the simulation and vary it parametrically. After this stage, the photoelectron count of each pixel is randomized according to the Poisson statistics including the random electron dark count that is added to each pixel. In this fashion, one obtains the final Earth's image plus noise in the focal plane array. Next the noisy image is digitized, or in other words the count of each pixel is digitized according to the number of digits of resolution of the analog-to-digital converter. The image that is now obtained is still affected by noise. In practice, the image in the focal plane is composed by the Earth's signal (plus noise) captured by a subset (or a sub-window) of pixels (e.g. NxN) and the rest of the pixels of the detector array containing the noise count only.

To effectively calculate the Earth's centroids in the image plane it was developed the following method. It was first located the Earth's sub-window of size NxN containing the Earth image located in (all) detector array of size MxM>NxN. To do so, we scan all the focal plane array using a sub-window of size of the order of the Earth disc. The sub-window with the largest photoelectron count contain the image of the Earth. The centroids of this sub-window is indicated as $\{\boldsymbol{x'},\boldsymbol{y'}\}$. Next, we calculate the centroiding of the Earth within the sub-window of interest. To have a correct calculation of the centroiding, we need to reduce the contribution of the overall background from the Earth' sub-window. To do so, we first estimate the an average pixel count (noise threshold) corresponding to the average pixel background count and then we subtract that noise threshold from each pixel in the Earth's sub-window. In the algorithm used, the pixel noise threshold is defined as the average count of the overall pixel array. Once we subtract the noise threshold from each pixel of the Earth's sub-window, one can perform the calculation of the Earth's centroids in the sub-window itself. To calculate the Earth's centroids in the Earth's sub-window containing NxN pixels we apply the center of mass relationship given by

$$\underline{x} = \frac{\sum_{i=1}^{N}\sum_{j=1}^{N} x_{ij}c_{ij}}{\sum_{i=1}^{N}\sum_{j=1}^{N} c_{ij}}; \quad \underline{y} = \frac{\sum_{i=1}^{N}\sum_{j=1}^{N} y_{ij}c_{ij}}{\sum_{i=1}^{N}\sum_{j=1}^{N} c_{ij}} \tag{1}$$

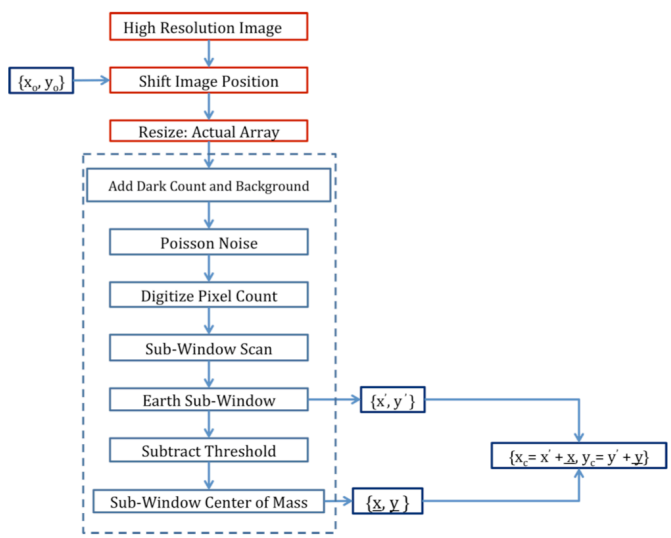

Figure 5. General sequence describing the centroiding algorithm. The dashed box includes only steps performed using the actual size detector array.

where $\underline{x}$ and $\underline{y}$ are the centroiding coordinates of the Earth within the Earth's sub-window, i and j are the indexes of the x and y axis, c_{ij} is the count of the ij pixel in the Earth's sub-window. If the Earth' sub-window centroidings are $\{\underline{x},\underline{y}\}$, the Earth centrodings will be then $\{ \boldsymbol{x_c} = \underline{x} + \boldsymbol{x'}, \boldsymbol{y_c} = \underline{y} + \boldsymbol{y'}\}$ that differ from the 'true' coordinate $\{x_o,y_o\}$, with centroid error $\{\varepsilon_x = x_o - \boldsymbol{x_c}\ ,\ \varepsilon_y = y_o - \underline{x}_{\boldsymbol{c}}\ \}$. The causes of possible centroid error can be several, including the Poisson noise of photodetection, the rendering of the Earth image in a 'coarse' pixel detector array, the effects of noise

background and dark count, and rounding due to analog to digital conversion. Also, to the spatial centroiding correspond the angles $\{\alpha_x , \alpha_y\}$ in elevation and azimuth that describe the offset of the optical system (telescope) from the Earth position in space defined as $\alpha_x=x_c/F$, $\alpha_y=y_c/F$, where F is the optical system focal length.

C. Input Parameters for the Earth acquisition and Centroiding algorithm.

The input parameters needed for the algorithm describing the Earth acquisition and centroiding calculation are presented in Table 1. These inputs parameters are defined as static because they cannot change during the (iterative) execution of the simulation. Discussion of the meaning of these input variables follows.

The strength of the signal from Earth's spectral radiance depends on the wavelength (Fig. 1) and the system optical bandwidth, rows 1, 12 and 13. The range (row 2 in the table) is the distance between Earth and spacecraft, the Earth FOV at the spacecraft decreases with the range. At the same time, the size of the image of the Earth on the focal plane decreases in size as the range increases. Inputs from row 3 to 5 in Table 1 briefly describe the optical system. The optical loss in the table (row 5) is the power loss that the Earth signal experiences in the path between the primary mirror of the telescope to the focal plane. Inputs from row 6 to 14 instead, describe the detector array performance parameters. We assume that the pixel quantum efficiency is uniform over the array. The central wavelength and the bandwidth define the spectral region where the Earth radiance is collected by the system. The bandwidth can be determined both by the detector spectral response and/or by an optical filter located in the optical path. The pixel saturation count is the pixel well depth. An analog-to-digital converter translates the pixel count in a integer number in the interval $\{0, 2^b-1\}$, where b it the bit resolution of the system (row 14). Regarding the issue of the technological availability of detector array in the thermal infrared, there are two main technological solutions available: quantum well infrared photodetector(s) (QWIP) [4] and Mercury Cadmium Telluride (HgCdTe) based photodetectors [5]. Initial runs of the simulation used basically data from QWIP detectors arrays found in the literature. Numbers in Table 1, therefore, refer to a QWIP sensor. However, future work will require a more accurate analysis to understand the characteristics of detector arrays in LWIR used in space programs, and most recent advances and characteristics of available detectors in LWIR spectrum.

Table 1. Example of Static Input of Earth Acquisition and Centroiding Algorithm for QWIP detector.

	Input (Dimensions)	Value
1	Earth Radiance ($W/cm^2/sr/\mu m$)	5E-4
2	Range (AU)	1
3	Aperture Size (cm)	20
4	System Focal Length (cm)	300
5	Optical Loss (dB)	3
6	Pixel Quantum Eff. (<1)	0.08
7	Pixel Dark Count (Kilo-Count/sec)	10
8	Pixel Size (μm)	10
9	Number Pixel (per Side)	100
10	Pixel Saturation Count	5E6
11	Pixel Count Gain	1
12	Central Wavelength (μm)	8.5
13	Bandwidth (μm)	1
14	Bit Resolution	16

IV. Line-of-sight Dynamic Model and Stabilization

In the following, we describe the dynamic model, the base body control, and the line-of-sight control used in the simulation. At each simulation step (the simulation update rate is 100 Hz), the simulation flow follows this sequence:

- Generates spacecraft (S/C) and gimbaled camera dynamic model,
- Generates S/C disturbances,
- Stabilizes S/C (base body) dynamics via PID control loop at 0.01 Hz,
- Computes S/C closed loop dynamics response.
- Applies SC response as disturbance to two-axis gimbaled payload (states= azimuth, elevation).
- Propagates the azimuth and elevation states of the camera dynamics
- Adds the sensor noise model to the computed azimuth and elevation states, based on the detector models and centroiding algorithm described above,
- Stabilizes line-of-sight via PID control at 100 Hz.
- goes to the next step.

This is summarized in Figure 6.

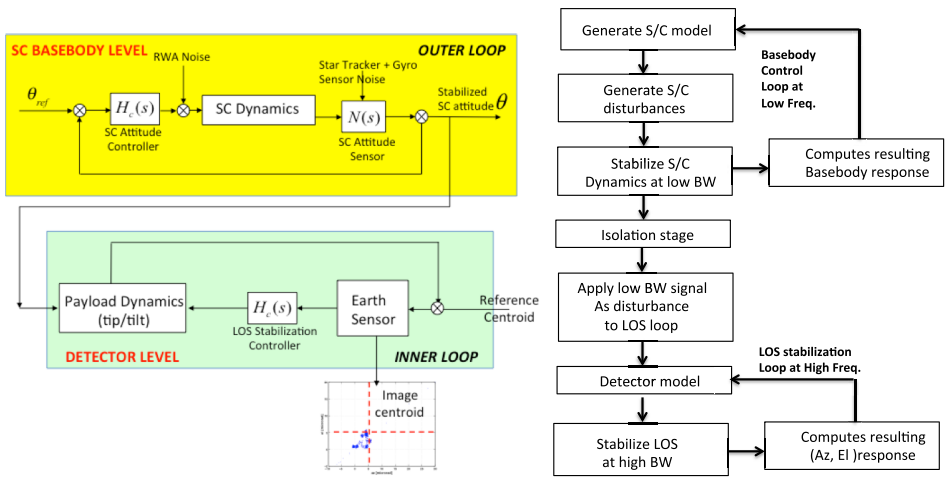

Figure 6. Simulation Model Block Diagram (right) and flow-chart (left).

The simulation assumes N uncoupled structural modes in second order form, and uses an exact solution to the harmonic oscillator equations in explicit form. The base body and camera models are described next. Hence, the disturbance is distributed to each oscillator in proportion to the load distribution matrix. This way, the solution is computationally fast.

D. Dynamic Model

An integrated modeling approach previously considered for high-precision space telescopes is followed in the development of the system model for control design [7]. The vehicle plant model is a model of the system in modal space, obtained from the system mass and stiffness matrix set. After solving the eigenvalue problem

$$K_a \Phi_a = \Lambda_a M_a \Phi_a \quad \text{with} \quad \Phi_a^T M_a \Phi_a = 1 \tag{2}$$

and introducing the canonical transformation $X_a = \Phi_a \eta_a$, where $\Phi_a = \begin{bmatrix} \Phi_1 & \cdots & \Phi_n \end{bmatrix}$ and there are n<N retained modes, we obtain the modal equations $\ddot{\eta}_a + \Lambda_a^2 \eta_a = \Phi_a^T D_a U_a$. These are the modal dynamics equations. Introducing now the structural damping matrix Σ, we may write:

$$\dot{Z}_a = \begin{bmatrix} 0 & 1 \\ -\Lambda_a^2 & -2\Sigma\Lambda_a \end{bmatrix} \begin{pmatrix} \eta_a \\ \dot{\eta}_a \end{pmatrix} + \begin{bmatrix} 0 \\ \Phi_a^T D_a \end{bmatrix} U_a = A_a Z_a + B_a U_a \tag{3}$$

The observation equations are $Y_a = \begin{bmatrix} \Phi_a & \Phi_a \end{bmatrix} Z_a$. The physical model at time step k can be written as

$$\ddot{\eta}_k + 2\Sigma\Lambda\dot{\eta}_k + \Lambda^2\eta = \Phi^T f_k \tag{4}$$

where Σ, Λ are diagonal (n x n) and η_k is the modal displacement, Φ is the modal matrix, and n is the number of retained modes. In state-space form, where A is (2nx2n) and B is (2nxn), this system becomes:

$$\begin{aligned} \dot{x}_k &= A\dot{x}_k + B_u u_k + B_w w_k \\ y_k &= C_y x_k + D_y u_k + v \\ z_k &= C_z x_k \end{aligned} \tag{5}$$

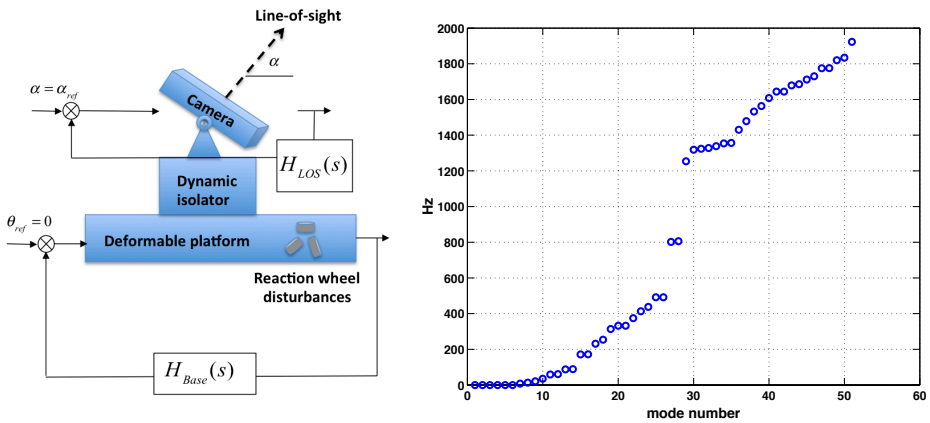

Figure 7. Dynamics model (left) and modal spectrum used for simulation (right).

where u_k is the actuator input, w_k is a disturbance input, and v is sensor noise, representative of the spacecraft gyro noise. B_w defines how the disturbances are input into the system, B_u defines how the actuator commands are input to the system, C_y relates the sensor outputs to the states, z are the performance outputs, C_z relates the performance outputs to the states, D_y relates the performance outputs to the control inputs, and y are the sensor outputs. The inputs and outputs of the model are defined based on the desired disturbances, performance outputs, and control systems. The nodal displacements, which are readily available using the FEM and mode shapes and we obtain:

$$
\begin{aligned}
A &= \begin{pmatrix} 0 & I \\ -\Lambda^2 & -2\Sigma\Lambda \end{pmatrix} \\
B &= \begin{pmatrix} 0 & \Phi^T \end{pmatrix}^T \\
x_k &= \begin{pmatrix} \eta_1 & \cdots & \eta_N & \dot{\eta}_1 & \cdots & \dot{\eta}_N \end{pmatrix}^T
\end{aligned}
\tag{6}
$$

It is assumed, as a default, that the modal damping is 0.001 uniformly for all modes, i.e., the structural damping is 0.1 % of critical, which is a typical assumption, at least for the lowest order modes . It is straightforward to modify the A matrix at a later time to change the damping, even on a mode-by-mode basis. This is done in many of the parametric studies performed using the integrated model.

If instead we assume that the base body is a rigid body, the state space model describing the dynamic of the system, stabilized by a proportional-derivative-integral (PID) controller is

$$
\begin{aligned}
\dot{x} &= Ax + Bu \\
y &= Cx + Du \\
A &= \left(0_{3x3}\right) \\
B &= \begin{pmatrix} 1_{3x3} & 0_{3x3} \end{pmatrix} \\
C &= JK_i \\
D &= \begin{pmatrix} JK_p & JK_v \end{pmatrix}
\end{aligned}
\tag{7}
$$

where the state x is given by $x = (q, \dot{q})$, with q=spacecraft attitude angles, y is the measurement used for feedback, u is the control input, K_p, K_v, and K_i are the PID control gains and J the spacecraft inertia. Consistent with the MRO data used below, the vehicle mass properties are as follows: Mass = 1271.88 kg, center of mass location in body

frame is r=(-0.024551,-1.251734,0.063671) m, moment of inertia matrix about the center of mass in body frame components is J =[2701.4 142.5 19.9;142.5 2640.6 -80.1; 19.9 -80.1 3967.2] kg m^2 .

E. Basebody Stabilization

The simulation involves an inner loop and an outer loop (see Figure 8). The objective of the outer loop is to stabilize the vehicle dynamics at low frequency. In Figure 8, the attitude error is first compensated at low frequency in the S/C attitude controller block. The objective of the base body stabilization control loop is to point the S/C at 0.01 Hz closed-loop bandwidth to achieve a micron-level pointing accuracy. In Figure 8, the transfer function

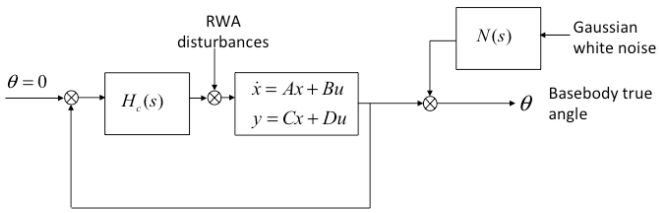

Figure 8. Basebody stabilization loop.

$$H_c(s) = \frac{s^3}{s^3 + 0.08796s^2 + 0.003948s + 4.5e-5} \tag{8}$$

models the base body controller at 0.01 Hz with 0.7 damping factor. The transfer function

$$N(s) = \frac{s}{s + 12.57} \tag{9}$$

models a representative gyro + star tracker noise with an undamped pole at 2 Hz. The control commands are then applied to the plant, which represents a linear state space model of the S/C dynamics, before being filtered by the sensor filter (gyro noise model).

F. Line-of-sight Stabilization

The objective of the inner loop is to do line-of-sight stabilization at high frequency. After the outer loop has stabilized the base body, the azimuth and elevation of the image figure are computed, and then sent to the model of the LWIR sensor, which returns a noisy version of these signals. These signals are then compared to the reference signal (zero) and used in a feedback loop which computes the corrective commands to return the (az,el) state back to the origin of the image plane.

The camera state space model describing the dynamic of the system is

$$\begin{aligned} \dot{x}_p &= A_p \dot{x}_p + B_p u_p + B_w w_p \\ y_p &= C_p x_p + D_p u_p + v_p \end{aligned} \tag{10}$$

where the (payload) camera state $x_p=(\theta,\dot{\theta})$, with θ=(azimuth angle, elevation angle), y is the measurement used for feedback, u_p is the control input and v_p is the sensor noise, described in Section III. The centroidal moments of inertia in azimuth and elevation are assumed to be equal to 2.0 kg m^2.

The disturbance w_c is considered to be the residual disturbance acting on the base body after base body stabilization. Furthermore, this disturbance is filtered by the dynamic isolation filter, described below.

The problem of line-of-sight stabilization can now be cast as an optimal control problem. A representative continuous time cost function can be expressed by $J_k = \int_{[0,\infty)} \left\{ \varepsilon_k^T Q_k \varepsilon_k + u_k^T R_k u_k \right\} dt$ where ε_k is the k-component of the error, Q_k is the weighting matrix associated with the error states to be defined, u_k are the control forces, applied to the azimuth and elevation channels that drive the error states along the three axes of motion, and R_k are appropriate input weighting matrices to be determined. The entries of the positive definite matrix Q_k are scaling factors that penalize error state deviations from zero to within specified requirements. For simplicity, these matrices can be chosen to be Q_k=[6.5 0;0 1e-6] and R_k=5e-7, for both azimuth and elevation, hence the error in position is penalized the most. Further, let the desired azimuth and elevation trajectories a_d, e_d. We can then write that the error along azimuth is $e_a=a-a_d$. The continuous-time optimal control laws for the a-axis is given by $u_a=-R_a^{-1}B_a^T P_a e_a$, where P_a are

the solutions to the matrix algebraic Riccati equations $0=P_aA+A^TP_a-P_aBR_a^{-1}B+H$, and similarly for the other axes. The existence and uniqueness of the optimal control solutions are established under the usual controllability and observability conditions. The control forces are constructed based on the relative error in the states. The optimal control gains thus obtained (3.6056e+03 Nm/rad in position and 38.0029 Nms/rad in velocity) are then used in the full state feedback loop, which has then a bandwidth of 266 Hz.

Figure 9 depicts the complete base body control and line of sight stabilization diagram.

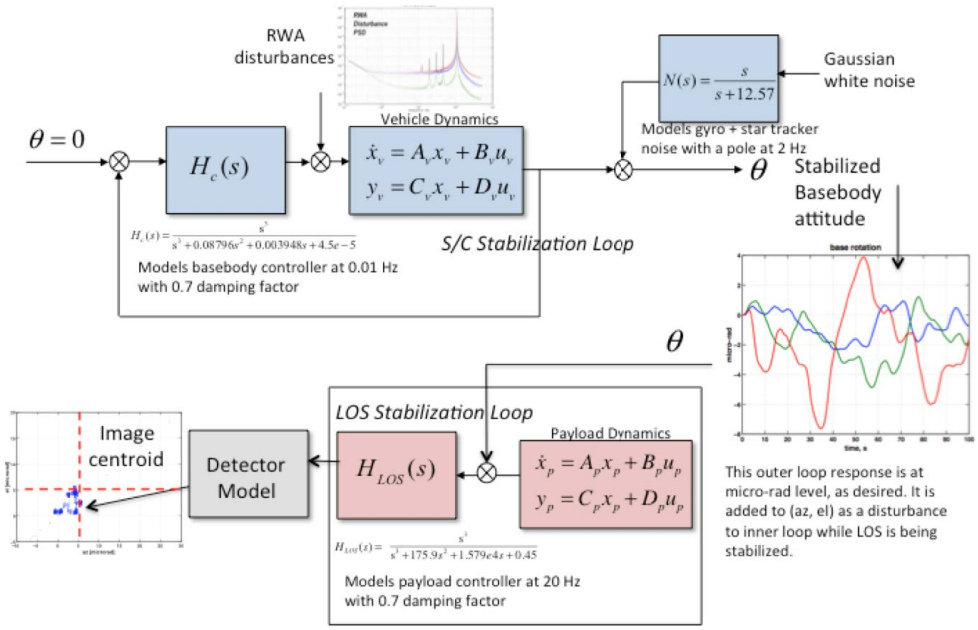

Figure 9. Spacecraft and LOS Stabilization Summary Diagram.

V. External Disturbances

Two sets of disturbances have been considered in the model an simulation effort. First, a set of reaction wheels that can apply imbalance forces and torques to the base-body have been used as disturbance source. Second, telemetered data from the Mars Reconnaissance Orbiter (MRO) has been used as a more realistic source of disturbances. These models are described next.

G. Reaction Wheels

A set of reaction wheels (typically running between -3000 and 3000 rpm) are added to the spacecraft base body, along the principal axes of the equivalent rigid body. They are a source of broadband disturbance which affects the line-of-sight jitter response. The disturbance model is such that the forces (i=1,2,3) and torques (i=4,5,6) associated with each wheel are composed of N harmonics of the form:

$$f_i(t) = \sum_{j=1}^{N} c_{ij}\Omega^2 \sin(h_j\Omega t + \phi_{ij}) \tag{11}$$

where Ω is the wheel speed and c_{ij} and h_j are known constants. The phases ϕ_{ij} are random variables uniformly distributed in $[-\pi,\pi]$. The wheel model is representative of Honeywell HR12 [9] wheels with a representative static balance (0.24 g cm), a representative dynamic imbalance (4.6 g cm^2), and with nominal wheel speed of +/- 3000 rpm. The model for the forces and torques due to wheel imbalance is as follows (η is a random number and ϕ is a random phase):

$$
\begin{aligned}
&w = 2\omega_{\max}\left(\eta - 0.5\right) \\
&\theta = wt + \phi \\
&F(t) = -w^2 b_1 \left[\sin\theta \quad \cos\theta \quad 0\right] \\
&T(t) = -w^2 b_2 \left[\sin\theta \quad \cos\theta \quad 0\right]
\end{aligned}
\tag{12}
$$

H. MRO Disturbances

As a more realistic source of disturbances, data from two phases of the MRO mission are used in this paper. This mission may serve as a useful proxy for future missions that might require high pointing accuracy payload such as an optical communications transceiver. To evaluate this motion actual ACS related flight data from the MRO spacecraft is used. These data were provided by Lockheed Martin of Boulder CO., designers of the MRO ACS, and reported in [8]. Numerous events during a given MRO orbit cause large pointing errors. These events include solar array gimbal changes, HGA gimbal changes, zero crossings of the reaction wheels, wheel desaturations, fuel slosh modes, and flexible appendage motion. The attitude control error signal was available at 5 Hz for both orbital data sets. Figure 10 shows time series of attitude control errors during successive orbit of Mars, and Table 2 summarizes the root mean squared pointing jitter during two representative orbits. These data were used to drive the base body disturbances in the simulations.

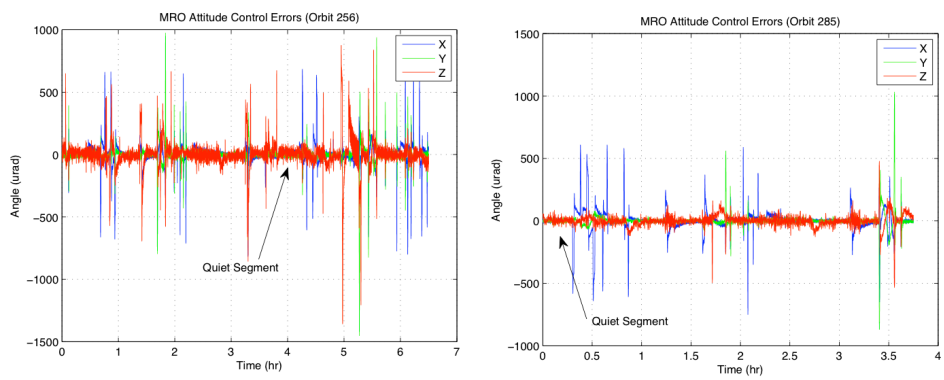

Figure 10. (a) MRO spacecraft RMS pointing jitter for cruise and orbit case.(b) Time series of attitude control errors during successive orbits of Mars.

Table 2. MRO Spacecraft RMS pointing jitter for cruise and orbit cases.

	X RMS (urad)	Y RMS (urad)	Z RMS (urad)
Cruise:	3.381	5.342	8.178
Orbit 256:	98.0	86.66	118.6
Orbit 256 (Quiet Segment):	12.44	12.81	28.1
Orbit 285:	95.4	55.44	43.58
Orbit 285 (Quiet Segment):	8.153	8.861	19.85

VI. Dynamic Isolation

At this time, the isolator is simply modeled as a 2nd order low pass filter along each one of the base body axes. Such a model is adequate for frequency-domain analysis, although for the simulation it is still useful to validate the results of the linear analysis. A more realistic model would account for mechanical cross-coupling between the 6 degrees-of-freedom. A transfer function for this simple filter model is of the form of a second order filter given by $G(s) = \omega_0^2 / (s^2 + 2\xi_0\omega_0 + \omega_0^2)$. The parameters ω_0 and ξ_0 define the characteristics of this filter; ω_0 is the natural frequency, and $\xi_0$is the damping. Devices employed in this application may be classified as passive (mechanical spring/damper), hybrid (passive plus electromechanical servo), or active (magnetic suspension). Reasonable assumptions for natural frequency and damping of the filter depend on the device type assumed. Passive devices will

exhibit lower damping, typically less than 5-10%, and natural frequencies generally 5 Hz or greater. Hybrid and active devices may be tuned to achieve higher damping, perhaps as high as 50%, and lower natural frequencies, perhaps as low as 0.1 Hz. However, sensor noise and actuator non-linearities will combine to limit performance of these devices.

Figure 11 shows the effect of changing the isolator corner frequency on the MRO power spectrum. Clearly, a 0.01 Hz corner frequency is more effective, but also it represents an isolation system that it is very difficult to realize. As a compromise, a corner frequency of 0.1 Hz was used in the simulations, which results in approx. one decade of attenuation above 0.1 Hz.

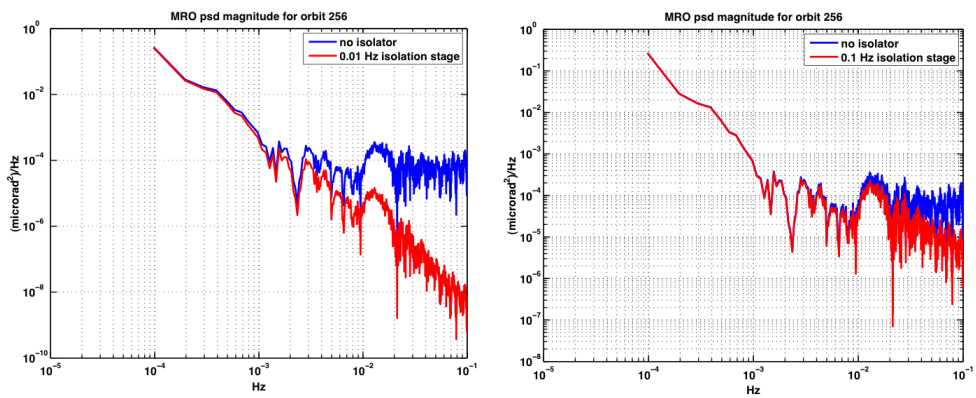

Figure 11. Effect of isolator corner frequency on MRO disturbance spectrum.

VII. Simulation Results and Discussion

Different sets of numerical experiments were done. In the first set of numerical experiments, only the reaction wheels were used as disturbances. The optical system static input were those indicated in Table 3. In this case, the initial condition in azimuth is 30 micro-rad, and in elevation 20 micro-rad. Figure 12 shows the system response before (left) and after (right) the LOS stabilization loop is closed, when the driving disturbance is noisy actuation by the reaction wheels. In this case, the LOS controller is not optimal, and there is no isolator stage, hence the dramatic difference. These figures indicate that, even in this case, the feedback loop achieves good steady state performance to within a few micro-radians in steady state after a brief transient, hence line-of-sight stabilization is achieved quickly. Figure 13 shows the comparison between the measured azimuth and elevation for a dark count of 4e5 Kilo-count/s (left) and 4e6 Kilo-count/s (right), indicating that a smaller dark count number affects the performance positively.

In the second set, the MRO data was used to synthesize a disturbance profile. In this case, the initial condition in azimuth is 700 micro-rad, and in elevation -700 micro-rad. A non-optimal proportional-derivative controller was implemented that would drive the system error to zero. Additional filtering of the incoming disturbances through an active isolation stage was required to further improve the steady state performance to sub-micron levels. In Figure 14, a long term simulation is carried out (10 seconds), the isolator is added, and the control errors (desired minus simulated) are observed to go to zero exponentially at steady state, as expected, while the feedback correction signals remain bounded, also as expected. The LOS stabilization feedback is turned on at the 1 second mark. The resulting (az,el) response at steady state once feedback loop is closed remains below 0.5 micro-radian, as shown in Fig. 15. These simulations were carried out with a representative QWIP detector, described above.

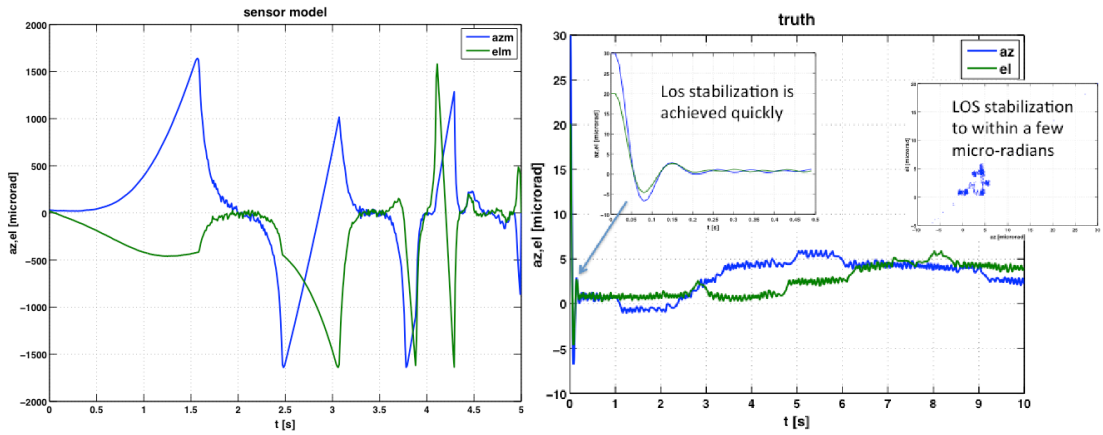

Figure 12. Comparison of azimuth and elevation in open loop (left) and stabilized LOS response (right). The driving disturbance is noisy actuation by reaction wheels.

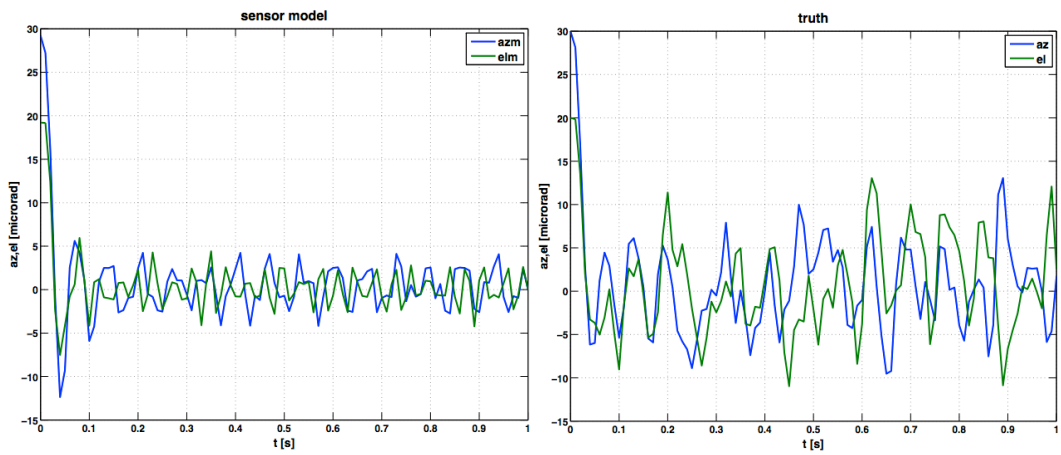

Figure 13. Measured Azimuth and elevation for a Dark Count of 4e5 Kc (left) and 4e6 Kc (right) for a QWIP detector.

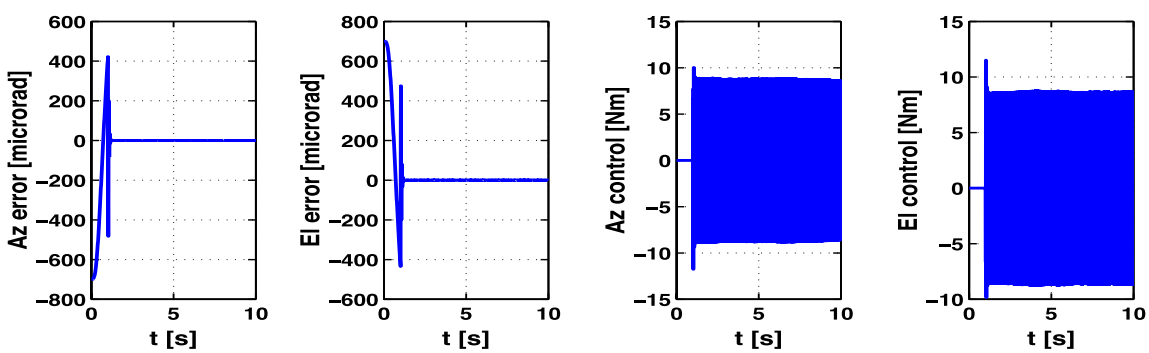

Figure 14. Azimuth and elevation errors and control effort for system with QWIP detector.

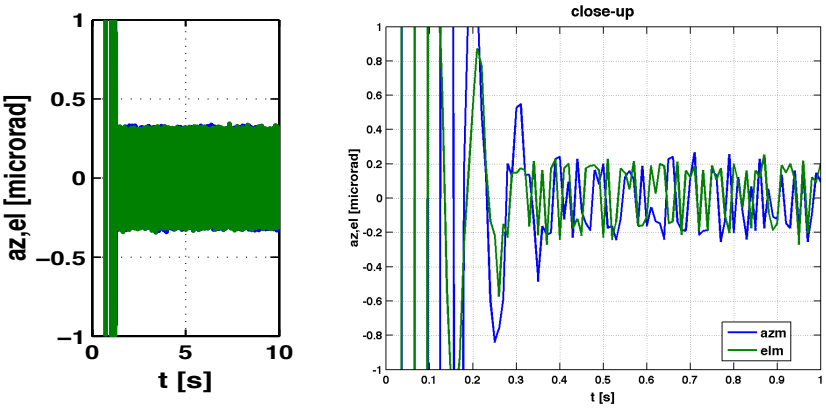

Figure 15. System response with QWIP detector in azimuth and elevation (left), and close-up (right).

In the third set, a comparison was made between the performance of a QWIP detector model and a HgCdTe detector model. The static parameters of these models is shown in Table 3. Again the MRO data was used in conjunction with the optimal controller, and the isolation stage, and the initial condition in azimuth was 300 micro-rad, and in elevation -100 micro-rad. Figure 16 shows the system response, indicating that a 0.2 micro-radian pointing accuracy is achieved with the QWIP detector model, while a 0.5 micro-radian accuracy is achieved with the HgCdTe detector model.

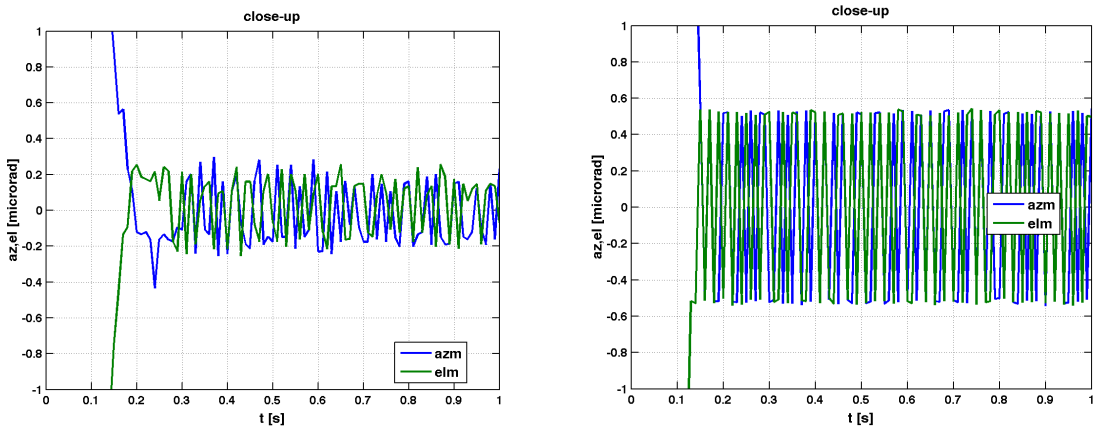

Figure 16. Close-up of response using QWIP detector model (left) and HgDcTe detector model (right).

Table 3. Representative static parameters for QWIP and HgCdTe detector models used in numerical experiments.

Input (Dimensions)	QWIP	HgCdTe
Earth Radiance (W/cm^2/sr/μm)	5E-4	5E-4
Range (AU)	1	1
Aperture Size (cm)	20	20
System Focal Length (cm)	300	470
Optical Loss (dB)	3	3
Pixel Quantum Eff. (<1)	0.08	0.7
Pixel Dark Count (Kilo-Count/sec)	400	1E5
Pixel Size (μm)	10	40
Number Pixel (per Side)	100	200
Pixel Saturation Count	5E6	50e6
Pixel Count Gain	1	1
Central Wavelength (μm)	8.5	11
Bandwidth (μm)	1	1
Bit Resolution	16	16

VIII. Conclusions

The objective of this study was to investigate the potential of using the bright and near-uniform Earth thermal infrared (or long wavelength infrared, LWIR) signature as a stable reference for accurate (µrad or less) inertial pointing and tracking of a telescope on a spacecraft including the determination of the fundamental limits of applicability of the proposed method for space missions. A comparison of the performance of QWIP (lower quantum efficiency, smaller spectral bandwidth, smaller dark count) and HgCdTe (higher quantum efficiency, larger spectral bandwidth, and lager dark count) using data from actual space qualified components was also carried out. In conclusion, preliminary results involving the effect of the sensor performance on the line-of-sight system stabilization have been described, and demonstrated that sub-microradian pointing accuracy is feasible.

Future work will involve the development of an integrated flight dynamics and control performance (Payload+Bus) engineering analyses and closed-loop simulations that provide system-level performance predictions for LOS Pointing Knowledge, Control, Stability, and Orbit Maneuvering. Analyses and simulations would verify pointing error budget allocations and determine pointing error margins with respect to current requirements. Some of the functions that have not been included in the present simulation are a state estimator, and a realistic model of the reference LOS to be tracked based on existing ephemerides. A more appropriate approach for LOS pointing and stabilization would also include: a) an outer stage Earth LOS sight tracking control loop at low frequency (milli-Hz), with an estimator (Kalman filter) that estimates LOS from ephemerides and navigation filter input, and a feedback controller on the S/C plant using reaction wheels for fine pointing; b) a medium stage LWIR image tracking/centroiding loop which, given estimated LOS and LWIR image on focal plane, estimates centroid offset; c) an inner stage LOS stabilization loop of centroid about LOS reference for disturbance rejection, which includes an estimator (Kalman filter) that takes centroid offset measurement and LOS and feeds back error to optical bench actuator, such as a fine steering mirror. Furthermore, more realistic actuator and sensor quantization and

nonlinearities should be included. Additionally, a realistic approach would also make use of a realistic dynamic isolation stage to effectively decouple the spacecraft motions from the optical bench motions. A model of the isolation system that effectively decouples the inner and outer loop needs to be developed. There are two methods to accomplish this goal: a) passive isolation, which reduces the mechanical coupling between S/C and platform, typically achieved by attaching the platform to the S/C using elastomeric mounts, and b) active cancellation, which applies feedback corrections to cancel pointing errors by adjust steering mirrors on the platform or applying corrective forces to the platform. While in the paper a simple dynamic isolator was considered, a goal of sub-micro radian LOS stabilization will likely require a combination or active and passive isolation, depending of the characterization of the disturbance environment. A parametric evaluation of the impact of the telescope size, focal length pixellation of the array for the better resolution/acquisition of the Earth image on the detector array, and inclusion of the background derived from the emission of the optical elements in the optical path and from contamination/mirror roughness induced stray light, should also be carried out. Finally, more realistic images of Earth (not longer as uniform disc) could leverage data from the Atmospheric Infrared Sounder (AIRS) mission, see Refs. [2] and [6].

Acknowledgments

The research described in this paper was carried out at the Jet Propulsion Laboratory, California Institute of Technology, under a contract with the National Aeronautics and Space Administration. Thanks to Dr. Joel Shields from JPL for providing the MRO data.

References

[1] G. Tinetti et al, 'Detectability of planetary characteristics in disk-averaged spectra II: synthetic spectra and light-curves of earth,' *Astrobiol* 6*(6):881-900* (2006).
[2] A.Biswas, S.Piazzolla, G.Peterson, G.G.Ortiz, and H.Hemmati, 'The Long-Wave Infrared Earth Image a Pointing Reference for Deep-Space Optical Communications,' IPN Progress Report 42-167 (2006).
[3] http://www.mathworks.com/products/matlab/.
[4] E. Costard, Ph. Bois, X. Marcadet, A. Nedelcu, 'QWIP and third generation IR imagers,' Proc. of SPIE Vol. 5978, 59781C (2005)
[5] P. Norton, 'HgCdTe Infrared Detectors,' Opto-Electronics Review 10(3), 159-174 (2002)
[6] www.airs.jpl.nasa.gov
[7] G. Mosier, M. fermiano, K. Ha, P. Bely, R. Burg, D. Redding, A. Kissil, J. Rackozy, L. Craig: "Fine Pointing and Control for a Next generation Space Telescope", Part of the SPIE Conference on Space Telescopes and Instruments, V, Kona, Hawaii•March1998.
[8] Shields, J., Srinivanas, M., Regher, M.: "Progress on the Development of a Simulation Environment for Optical Communications," Free-Space Laser Communication Technologies XXIV, edited by Hamid Hemmati, Don M. Boroson, Proc. of SPIE Vol. 8246, 82460X, · doi: 10.1117/12.913567.
[9] http://www51.honeywell.com/aero/common/documents/Constellation_Series_Reaction_Wheels.pdf